Supporting Information

Enhancing p-type thermoelectric performances of polycrystalline SnSe via tuning phase transition temperature

Yong Kyu Lee,[†,‡] Kyunghan Ahn,[‡] Joonil Cha,[†,‡] Chongjian Zhou,[‡] Hyo Seok Kim,[‡] Garam Choi,[‡] Sue In Chae,[†,‡] Jae-Hyuk Park,[†,‡] Sung-Pyo Cho,[§] Sang Hyun Park,[∥] Yung-Eun Sung,[†,‡] Won Bo Lee,[‡] Taeghwan Hyeon,[†,‡] In Chung [*,†,‡]

[†]*Center for Nanoparticle Research, Institute for Basic Science (IBS), Seoul 08826, Republic of Korea.*

[‡]*School of Chemical and Biological Engineering and Institute of Chemical Processes, and* [§]*National Center for Inter-University Research Facilities, Seoul National University, Seoul 08826, Republic of Korea.*

[∥] *Advanced Materials and Devices Laboratory, Korea Institute of Energy Research, Daejeon 34129, Republic of Korea.*

* To whom correspondence should be addressed: inchung@snu.ac.kr

List of Contents

Table S1. Chemical compositions of the samples of $Sn_{1-x}Pb_xSe$ (x = 0, 0.05, 0.1, 0.15, 0.2) and $Na_{0.01}(Sn_{1-x}Pb_x)_{0.99}Se$ (x = 0, 0.05, 0.1, 0.15, 0.2) analyzed by electron probe micro-analysis (EPMA) and inductively coupled plasma atomic emission spectroscopy (ICP-AES). Standard deviation for analyzed compositions is given.

Nominal compositions	Analyzed compositions (EPMA+ICP-AES)
SnSe	$SnSe_{1.013(4)}$
$Sn_{0.95}Pb_{0.05}Se$	$Sn_{0.95}Pb_{0.051(1)}Se_{1.02(2)}$
$Sn_{0.9}Pb_{0.1}Se$	$Sn_{0.9}Pb_{0.100(1)}Se_{1.01(1)}$
$Sn_{0.85}Pb_{0.15}Se$	$Sn_{0.85}Pb_{0.152(1)}Se_{1.01(1)}$
$Sn_{0.8}Pb_{0.2}Se$	$Sn_{0.8}Pb_{0.199(2)}Se_{1.01(2)}$
$Na_{0.01}Sn_{0.99}Se$	$Na_xSn_{0.99}Se_{1.01(1)}$
$Na_{0.01}(Sn_{0.95}Pb_{0.05})_{0.99}Se$	$Na_{0.010(1)}(Sn_{0.95}Pb_{0.050(1)})_{0.99}Se_{1.01(2)}$
$Na_{0.01}(Sn_{0.9}Pb_{0.1})_{0.99}Se$	$Na_{0.010(1)}(Sn_{0.9}Pb_{0.100(1)})_{0.99}Se_{1.00(3)}$
$Na_{0.01}(Sn_{0.85}Pb_{0.15})_{0.99}Se$	$Na_{0.010(1)}(Sn_{0.85}Pb_{0.149(1)})_{0.99}Se_{1.00(2)}$
$Na_{0.01}(Sn_{0.8}Pb_{0.2})_{0.99}Se$	$Na_{0.010(1)}(Sn_{0.8}Pb_{0.192(3)})_{0.99}Se_{1.01(1)}$

Table S2. Apparent density of the samples of $Sn_{1-x}Pb_xSe$ (x = 0, 0.05, 0.1, 0.15, 0.2) and $Na_{0.01}(Sn_{1-x}Pb_x)_{0.99}Se$ (x = 0, 0.05, 0.1, 0.15, 0.2).

Nominal compositions	Density (g/cm^3)
SnSe	5.978
$Sn_{0.95}Pb_{0.05}Se$	6.190
$Sn_{0.9}Pb_{0.1}Se$	6.390
$Sn_{0.85}Pb_{0.15}Se$	6.445
$Sn_{0.8}Pb_{0.2}Se$	6.548
$Na_{0.01}Sn_{0.99}Se$	5.893
$Na_{0.01}(Sn_{0.95}Pb_{0.05})_{0.99}Se$	6.072
$Na_{0.01}(Sn_{0.9}Pb_{0.1})_{0.99}Se$	6.228
$Na_{0.01}(Sn_{0.85}Pb_{0.15})_{0.99}Se$	6.326
$Na_{0.01}(Sn_{0.8}Pb_{0.2})_{0.99}Se$	6.468

Table S3. Comparison of electrical conductivity for $Na_{0.01}(Sn_{1-x}Pb_x)_{0.99}Se$ (x = 0, 0.03, 0.04, 0.05, 0.06) at 300 K and 773 K.

Nominal compositions	σ_{300K} (S cm^{-1})	σ_{773K} (S cm^{-1})
$Na_{0.01}Sn_{0.99}Se$	53	67
$Na_{0.01}(Sn_{0.97}Pb_{0.03})_{0.99}Se$	30	79
$Na_{0.01}(Sn_{0.96}Pb_{0.04})_{0.99}Se$	41	90
$Na_{0.01}(Sn_{0.95}Pb_{0.05})_{0.99}Se$	59	91
$Na_{0.01}(Sn_{0.94}Pb_{0.06})_{0.99}Se$	25	93

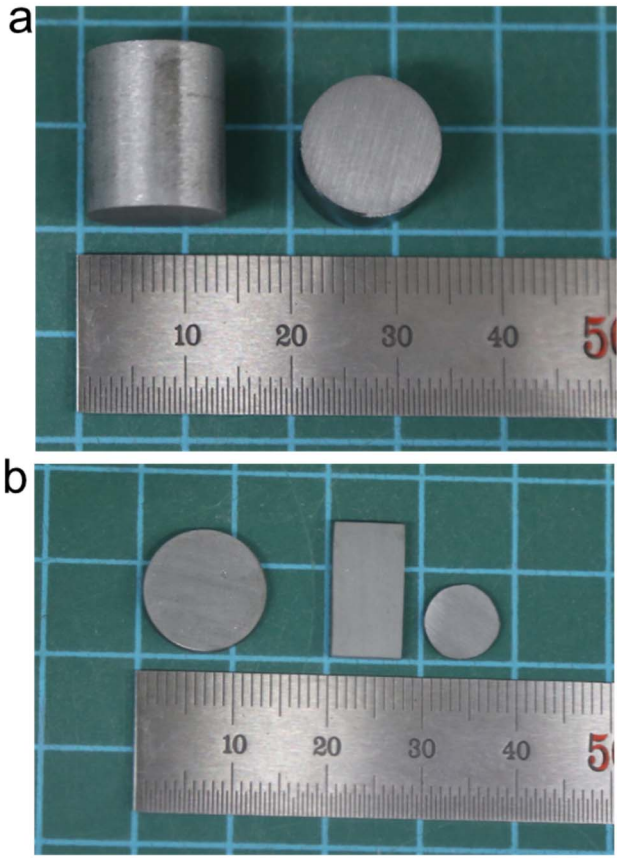

Figure S1. (a) Typical dense pellet by SPS with a typical diameter of 13 mm and a height of ~15 mm to 16 mm and (b) specimens cut for measuring electrical (disk for measuring perpendicular to pressing direction, left) (bar for measuring along the pressing direction, middle) and thermal transport properties (disk, right).

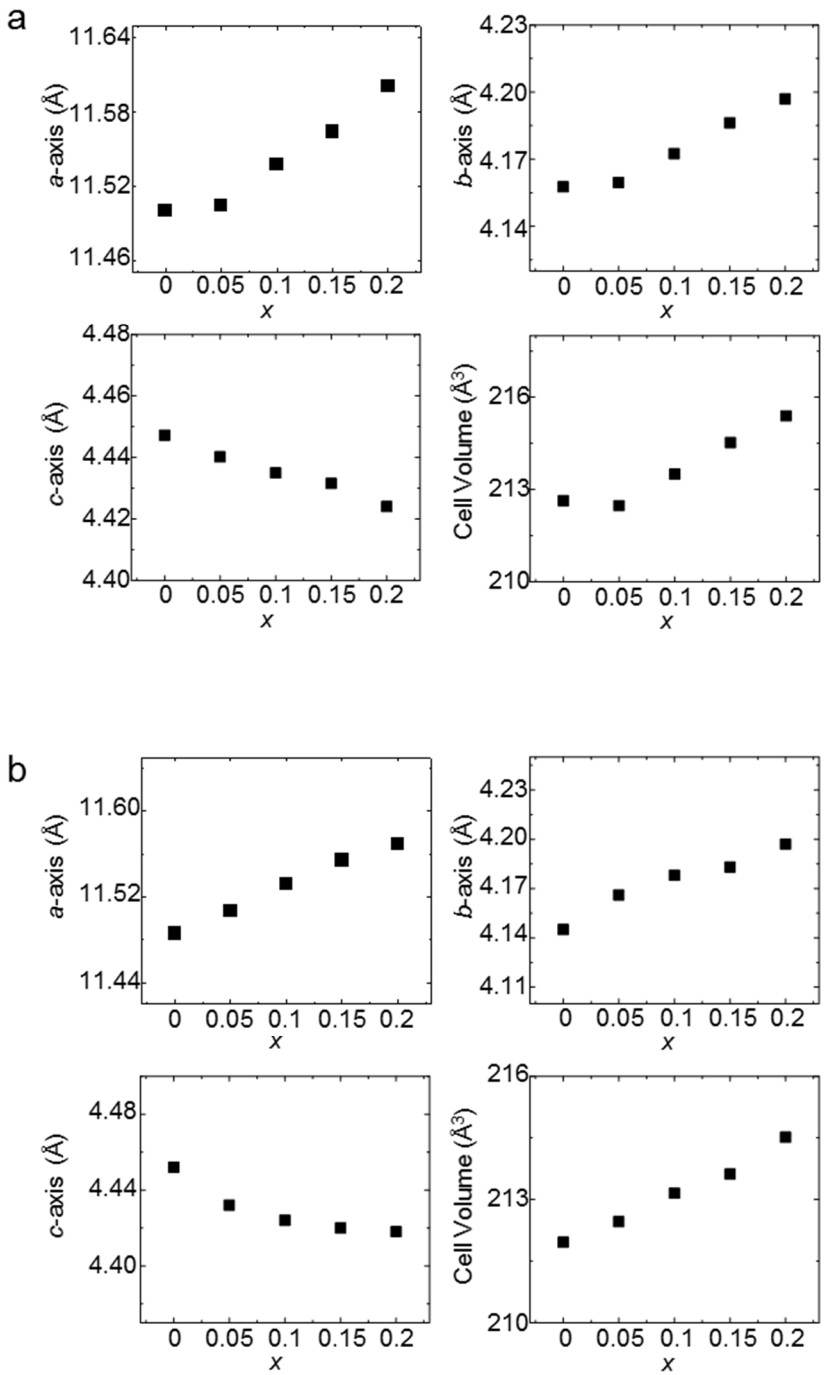

Figure S2. Lattice parameters and cell volume as a function of x for (a) $Sn_{1-x}Pb_xSe$ (x = 0, 0.05, 0.1, 0.15, 0.2) and (b)$Na_{0.01}(Sn_{1-x}Pb_x)_{0.99}Se$ (x = 0, 0.05, 0.1, 0.15, 0.2).

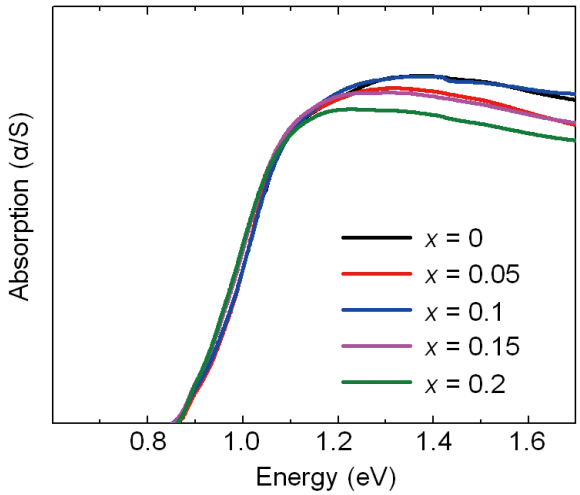

Figure S3. Optical absorption spectra of $Sn_{1-x}Pb_xSe$ (x = 0 – 0.2)

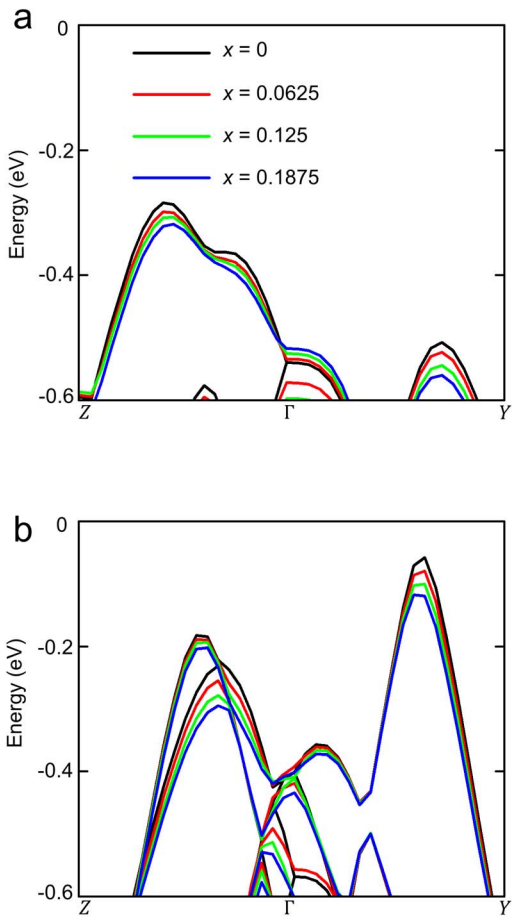

Figure S4. Electronic structures for (a) *Pnma* and (b) *Cmcm* of $Sn_{1-x}Pb_xSe$ ($x = 0$, 0.0625, 0.125, 0.1875) focused on the valence band maxima.

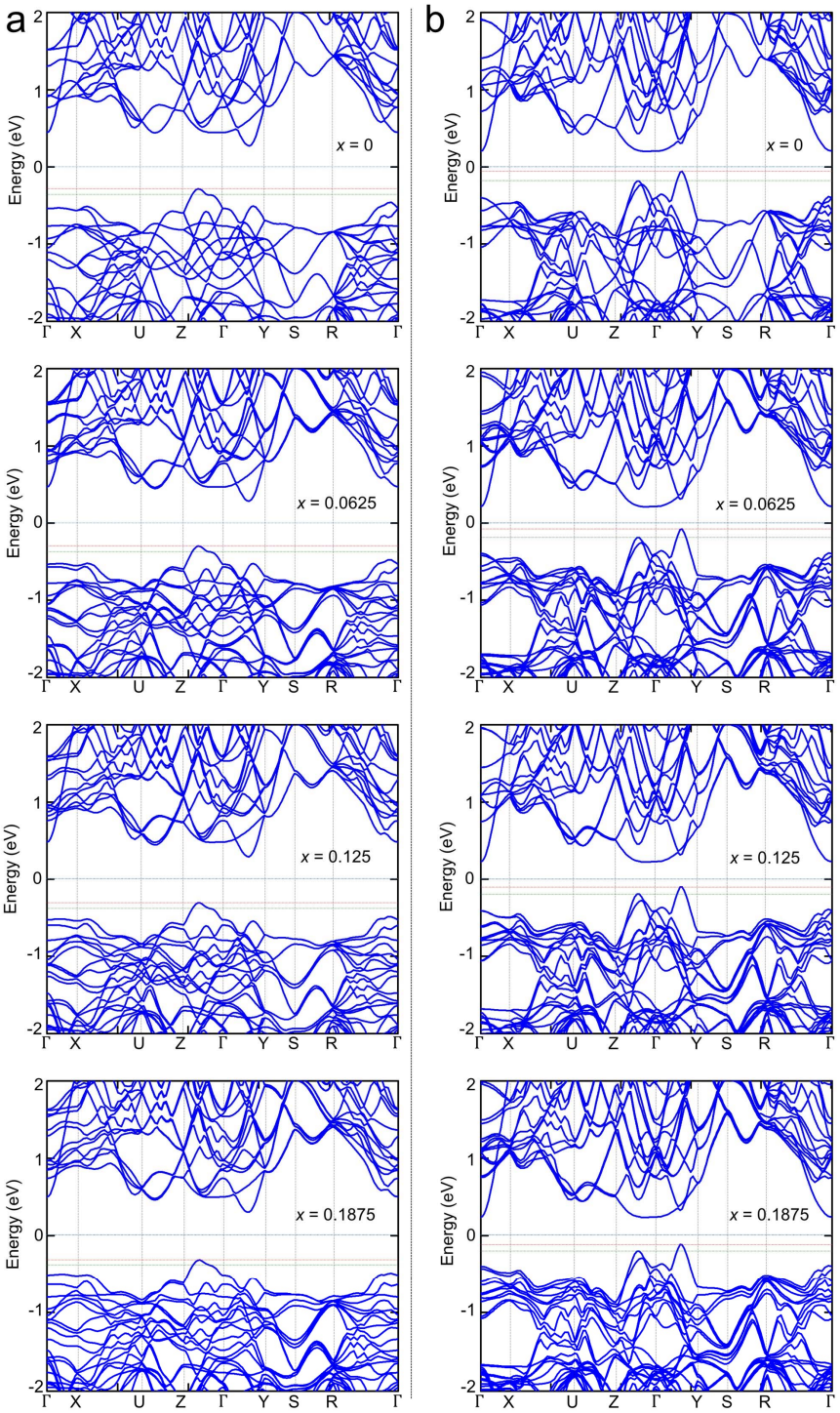

Figure S5. Electronic structures for (a) *Pnma* and (b) *Cmcm* phases of $Sn_{1-x}Pb_xSe$ (x = 0, 0.0625, 0.125, 0.1875)

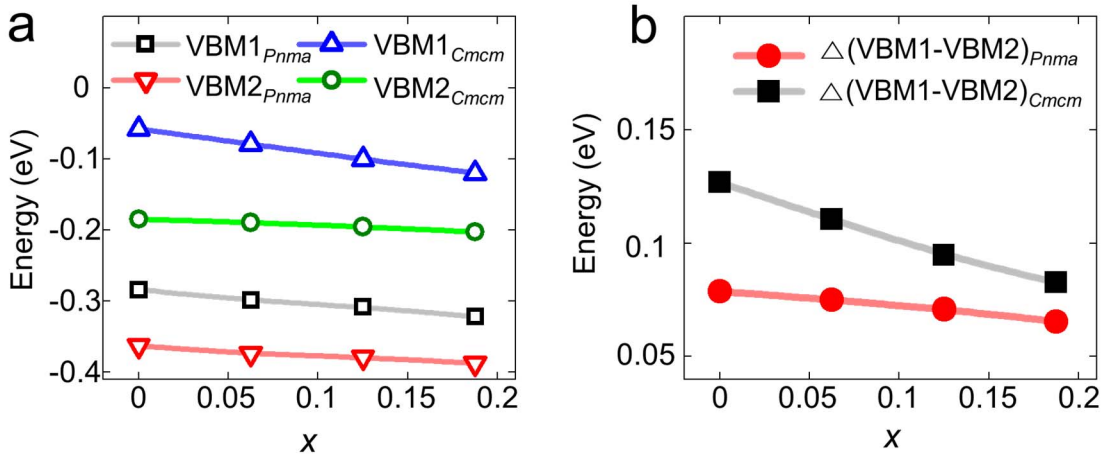

Figure S6. (a) The energy variations of the valence band maxima and (b) their differences as a function of x for $Sn_{1-x}Pb_xSe$ (x = 0, 0.0625, 0.125, 0.1875)

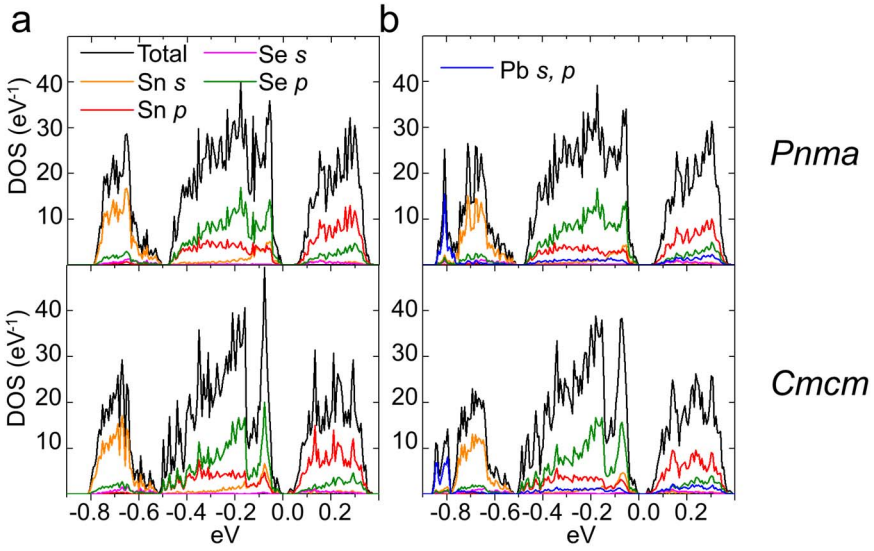

Figure S7. The projected density of states of *Pnma* and *Cmcm* phases of (a) SnSe and (b) $Sn_{0.8125}Pb_{0.1875}Se$

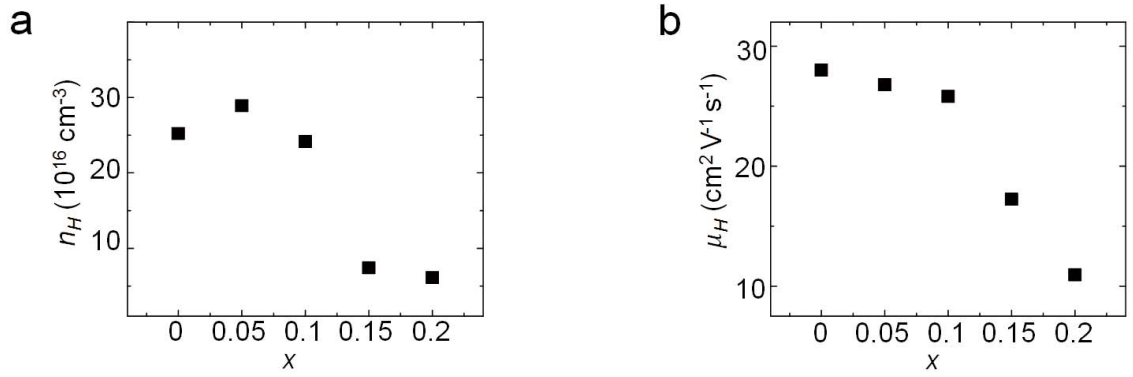

Figure S8. (a) Hall carrier concentration and (b) mobility at room temperature as a function of x for $Sn_{1-x}Pb_xSe$ (x = 0, 0.05, 0.1, 0.15, 0.2).

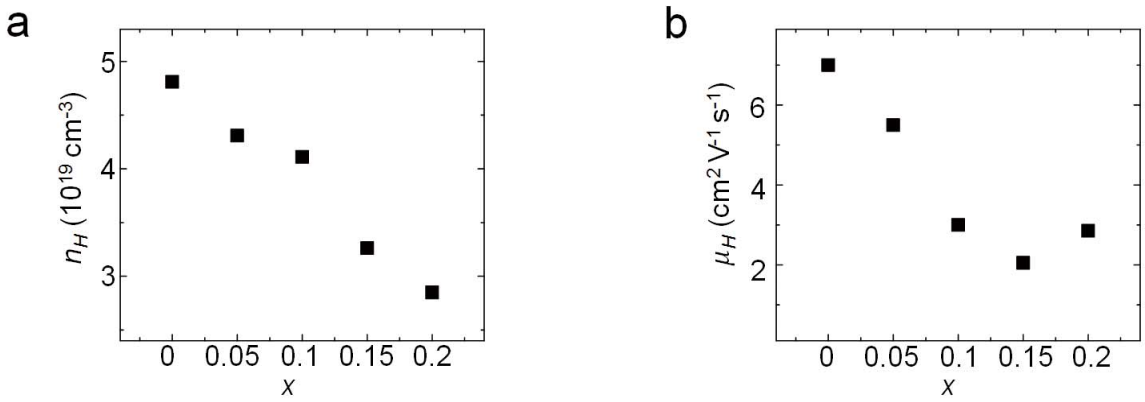

Figure S9. (a) Hall carrier concentration and (b) mobility at room temperature as a function of x for $Na_{0.01}(Sn_{1-x}Pb_x)_{0.99}Se$ (x = 0, 0.05, 0.1, 0.15, 0.2).

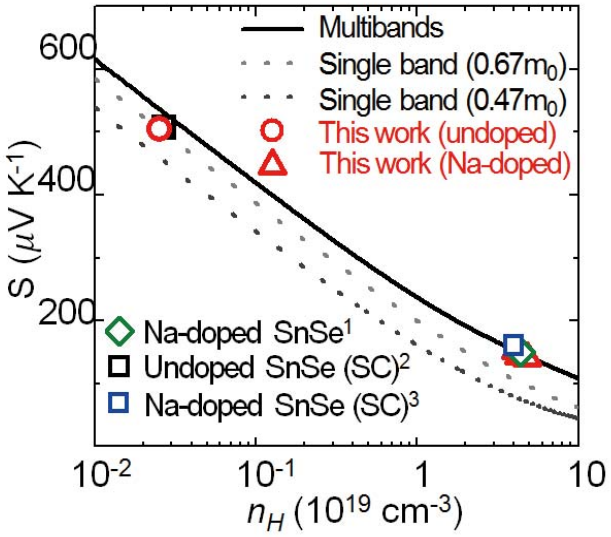

Figure S10. Seebeck coefficient as a function of hole concentration (n_H) at room temperature.

We calculated the Pisarenko relation between S and n_H using a single parabolic band (SPB) and a multivalley band (MVB) models for SnSe, and compared the results with the experimental S values at 300 K for $Sn_{0.95}Pb_{0.05}Se$ and $Na_{0.01}(Sn_{0.95}Pb_{0.05})_{0.99}Se$ in this work as well as for the previous reports.[1-3] The S values for undoped samples from this (i.e. $Sn_{0.95}Pb_{0.05}Se$) and the previous work[2] are well fitted by the SPB model with the effective mass of $m = 0.67m_0$ (m_0: free electron mass). In contrast, those for Na-doped samples are close to the MVB model, suggesting that the presence of multiple valleys in the valence band plays an important role in Seebeck coefficients for this heavily doped system as reported previously.[1,3] Since only 0.02 eV differs between the first light and heavy valence bands, the activated heavy valence band by hole doping can push the Fermi level down.[3] However, PbSe alloying marginally affects S values, which is consistent with the results of our electronic structure calculations showing that it negligibly disturbs the VBM.

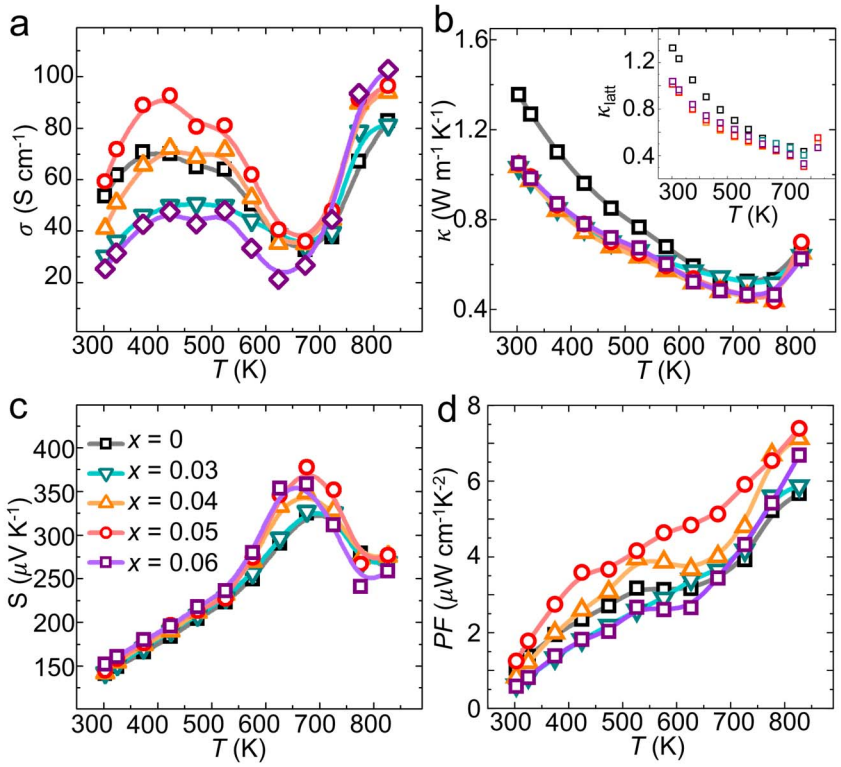

Figure S11. Temperature dependence of (a) electrical conductivity, (b) total thermal conductivity, (d) Seebeck coefficient, and (e) Power factor of $Na_{0.01}(Sn_{1-x}Pb_x)_{0.99}Se$ (x = 0, 0.03 – 0.06).

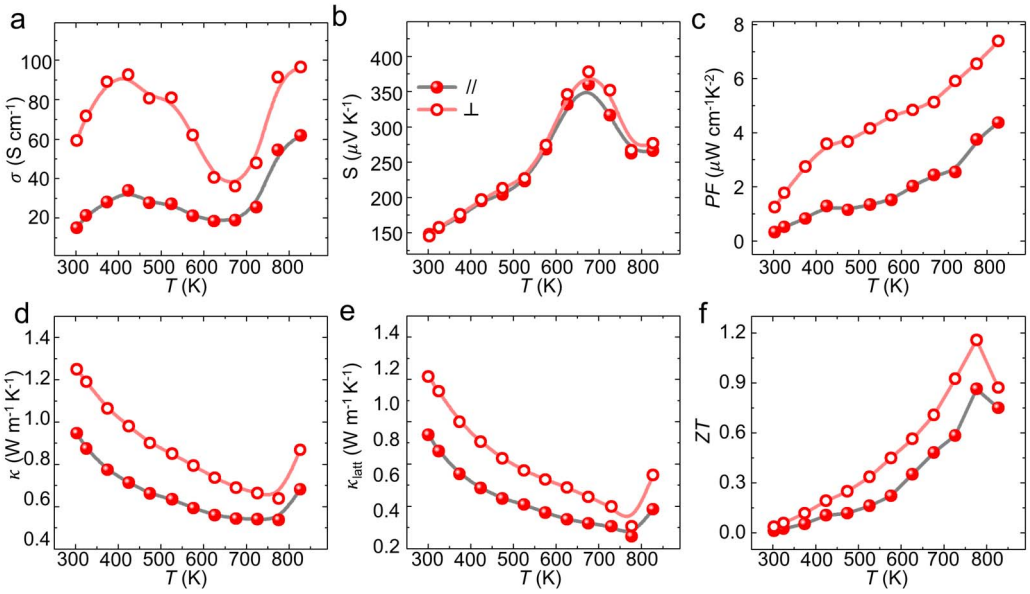

Figure S12. Temperature dependence of (a) electrical conductivity, (b) Seebeck coefficient, (c) power factor, (d) total thermal conductivity, (e) lattice thermal conductivity, and (f) figure of merit *ZT* of $Na_{0.01}(Sn_{0.95}Pb_{0.05})_{0.99}Se$ measured parallel (//) and perpendicular to the press direction (⊥) of spark plasma sintering.

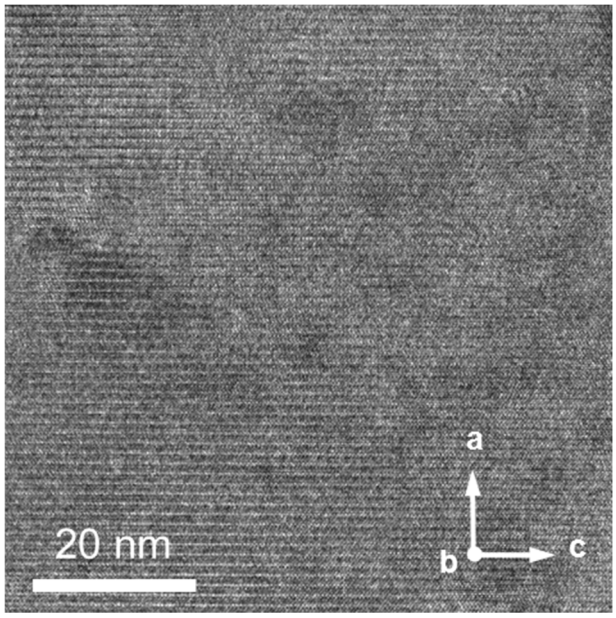

Figure S13. Cross-sectional bright-field scanning TEM image of the $Sn_{0.96}Pb_{0.04}Se$ sample showing nanostructures embedded inside the matrix.

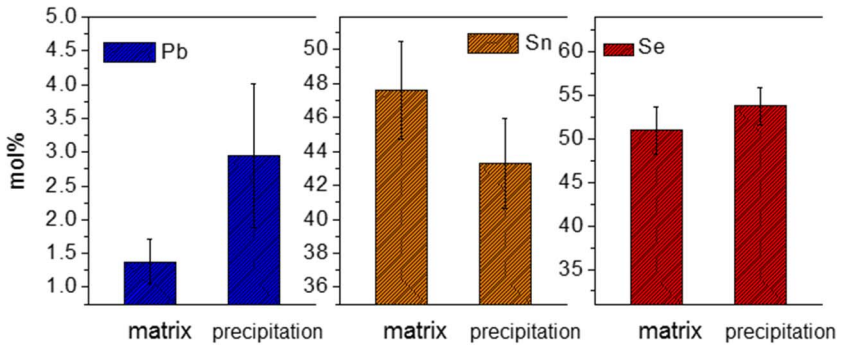

Figure S14. Elemental analysis on nanostructures and their surrounding matrix in the $Na_{0.01}(Sn_{0.96}Pb_{0.04})_{0.99}Se$ sample by STEM-EDS.

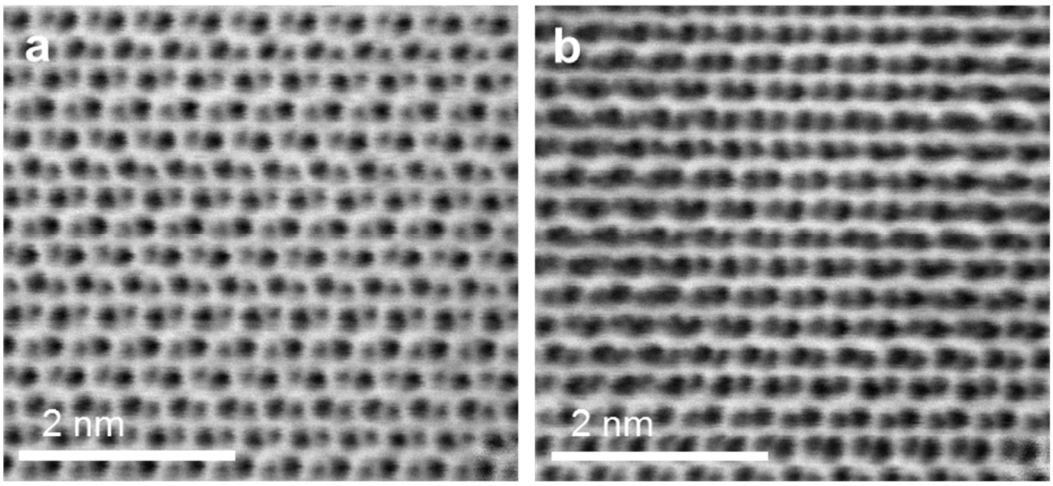

Figure S15. High-magnification atomic-resolution annular bright-field STEM image focusing on (a) the matrix and (b) the nanodot therein.

2. Calculation details for pisarenko plot

Relationship between Seebeck coefficients and carrier concentrations was modeled by multiple and single parabolic band models, respectively, for better understanding variations of electronic structures by doping and alloying processes by the following equations[4]:

$$n_i = 1/3\pi^2 \left[2m_i^* k_B T/\hbar^2\right]^{3/2} {}^0F_0^{3/2}(\eta_i,\beta_i) \quad \cdots \text{ [eq.1]}$$

$$S_i = k_B/e \left[{}^1F_{-2}^1(\eta_i-\Delta_i,0)/ {}^0F_{-2}^1(\eta_i-\Delta_i,0) - (\eta-\Delta_i)\right] \quad \cdots \text{ [eq.2]}$$

$$\mu_i = \frac{2\pi h^4 e\, C_i}{m_i^*(2m_d^* k_B T)^{3/2} E_{def}^2} \frac{{}^0F_{-2}^1(\eta_i,\beta_i)}{{}^0F_0^{3/2}(\eta_i,\beta_i)} \quad \cdots \text{ [eq.3]}$$

$$S_{total} = \sum \sigma_i S_i/\sigma_i \quad \cdots \text{ [eq.4]}$$

$${}^nF_m^k(\eta,\beta) = \int_0^\infty [-\partial f/\partial\varepsilon]\varepsilon^n(\varepsilon+\alpha\varepsilon^2)^k[(1+2\alpha\varepsilon)^2+2]^{m/2} d\varepsilon \cdots \text{ [eq.5]}$$

Apparently, the above equations represent the single parabolic band model if i =1.

3. Calculation details regarding lattice thermal conductivity

Based on the Callaway-Debye model, we calculated the temperature-dependent lattice thermal conductivity using the following equations:

$$\kappa_{latt}=\frac{k_B}{2\pi^2 v}\left(\frac{k_B T}{\hbar}\right)^3\int_0^{\theta_a/T}\tau_{tot}(x)\,\frac{x^4 e^x}{(e^x-1)^2}\,dx$$

τ_{tot} is the total relaxation time, which is given by

Umklapp Phonon scattering:[5]

$$\tau_U^{-1}=A_N*\frac{2}{(6\pi^2)^{1/3}}\frac{k_B\bar{V}^{1/3}\gamma^2\omega^2 T}{\bar{M}v^3}$$

Point defects scattering:[6,7]

$$\tau_{PD}^{-1}=\frac{\bar{V}\omega^4}{4\pi v^3}*\sum(1-x_i)\left[\left(\frac{M_i-M}{M}\right)^2+\varepsilon\left(\frac{a_i-a}{a}\right)^2\right]$$

Nano-precipitation scattering:[8]

$$\tau_{pre}^{-1}=v*\left[\left(2\pi R^2\right)^{-1}+\left(\frac{4}{9}\pi R^2\left(\Delta D/D\right)^2\left(\frac{\omega R}{v}\right)\right)^4\right]^{-1}*N_p$$

As confirmed by STEM studies, significant dislocations are present in our samples. Their effect also must be considered. The relaxation time of dislocations consists of both a dislocation core and dislocation strain effects as follows:[9]

$$\tau_{DC}^{-1}=\frac{N_D\bar{V}^{4/3}\omega^3}{v^2}$$

$$\tau_{DS}^{-1}=A*B_D^2\gamma^2\omega\left[\frac{1}{2}+\frac{1}{24}\left(\frac{1-2r}{1-r}\right)^2\left(\left(1+\sqrt{2}\left(\frac{v_L}{v_T}\right)^2\right)^2\right)\right]$$

Note: k_B is the Boltzmann constant, v is the average sound speed, $\hbar$ is the Plank constant, θ_a is the Debye temperature, T is the absolute temperature, γ is the Grüneisen parameter, $\bar{M}$ is the average molar mass, A_N is the fitting parameter for normal process, a_i is the radius of impurity atom in host matrix, x_i is the ratio of point defects, M_i is the impurity's atom mass, and ε is a phenomenological factor as a function of Grüneisen parameter. The structural parameters such as a radius and density of nanostructures were acquired from STEM analysis from this work. Other parameters were obtained from the previous literatures on thermal transport calculations.[10,11] These parameters were used to calculate the theoretical lattice thermal conductivity with various scattering process conditions. The calculated results were compared with our experimental values. All the parameters used are given in Table S4 and reference.[11]

Figure 10 in the manuscript shows the calculated κ_{latt} with application of various scattering mechanisms in comparison with the experiment values for the samples of pristine SnSe, Pb

alloyed $Sn_{0.95}Pb_{0.05}Se$, Na doped and Pb alloyed $Na_{0.01}(Sn_{0.95}Pb_{0.05})_{0.99}Se$. U and PD represent the Umklapp scattering and point defect scattering model, respectively. For the pristine SnSe sample, the calculated κ_{latt} curve based on the U model agrees well the experiment data. For the Pb alloyed sample, substituted Pb atoms are assumed to behave as point defects at relatively low temperature, and the U+PD model quantitatively predicts its experiment data. However, the significant deviation between the calculated and the experiment values occurs with increasing temperature mainly due to gradual disappearance of mass fluctuation given by Pb point defects in high temperatures.

For Na doped and Pb alloyed samples, experimental values are located well below the κ_{latt} curve based on the U+PD model over the entire temperature range, indicating emerging multiple phonon scatterings. With consideration of both nanostructuring and dislocations observed in STEM studies in this work as the significant source of phonon scattering, our model fits well with experimental values. As a consequence, the synergistic effect of nanostructuring and dislocations could be the main reason of the reduced κ_{latt} observed for Na-doped and Pb-alloyed samples, rather than single point defect scattering.

Table S4. Parameters used for calculating lattice thermal conductivities

Parameters	Symbol	Unit	SnSe
Space group			*Pnma*
Lattice constant	*a, b, c*	Å	*a*=11.491, *b*=4.15, *c*=4.44
Debye Temperature	θ_D	K	107
Sound velocity	υ	m s^{-1}	1674
Grüneisen parameter	γ		2.65
Phenomenological factor	ε		125

References

(1) Wei, T.-R.; Tan, G.; Zhang, X.; Wu, C.-F.; Li, J.-F.; Dravid, V. P.; Snyder, G. J.; Kanatzidis, M. G. *J. Am. Chem. Soc.* **2016**, *138*, 8875-8882.

(2) Zhao, L.-D.; Lo, S.-H.; Zhang, Y.; Sun, H.; Tan, G.; Uher, C.; Wolverton, C.; Dravid, V. P.; Kanatzidis, M. G. *Nature* **2014**, *508*, 373-377.

(3) Zhao, L.-D.; Tan, G.; Hao, S.; He, J.; Pei, Y.; Chi, H.; Wang, H.; Gong, S.; Xu, H.; Dravid, V. P.; Uher, C.; Snyder, G. J.; Wolverton, C.; Kanatzidis, M. G. *Science* **2016**, *351*, 141-144.

(4) Zhang, Q.; Liao, B.; Lan, Y.; Lukas, K.; Liu, W.; Esfarjani, K.; Opeil, C.; Broido, D.; Chen, G.; Ren, Z. *Proc. Natl. Acad. Sci.* **2013**, *110*, 13261-13266.

(5) Toberer, E. S.; Zevalkink, A.; Snyder, G. J. *J. Mater. Chem.* **2011**, *21*, 15843-15852.

(6) Wang, H.; LaLonde, A. D.; Pei, Y.; Snyder, G. J. *Adv. Funct. Mater.* **2013**, *23*, 1586-1596..

(7) Abeles, B. *Phys. Rev.* **1963**, *131*, 1906.

(8) He, J.; Girard, S. N.; Kanatzidis, M. G.; Dravid, V. P. *Adv. Funct. Mater.* **2010**, *20*, 764-772.

(9) Kim, S. I.; Lee, K. H.; Mun, H. A.; Kim, H. S.; Hwang, S. W.; Roh, J. W.; Yang, D. J.; Shin, W. H.; Li, X. S.; Lee, Y. H. *Science* **2015**, *348*, 109-114.

(10) Wei, T.-R.; Tan, G.; Wu, C.-F.; Chang, C.; Zhao, L.-D.; Li, J.-F.; Snyder, G. J.; Kanatzidis, M. G. *Appl. Phys. Lett.* **2017**, *110*, 053901.

(11) Wei, T.-R.; Wu, C.-F.; Zhang, X.; Tan, Q.; Sun, L.; Pan, Y.; Li, J.-F. *Phys. Chem. Chem. Phys.* **2015**, *17*, 30102-30109.